Predictions of microstructure and stress in planar extensional flows of a dense viscous suspension

Predictions of microstructure and stress in two-dimensional pure shearing of a dense viscous suspension

James T. Jenkins[1] †, Ryohei Seto[2] and Luigi La Ragione[3]

[1]School of Civil and Environmental Engineering, Cornell University, Ithaca, NY 14853, USA

[2]Wenzhou Institute, University of Chinese Academy of Sciences, Wenzhou, Zhejiang, CN

[3]Dipartimento di Scienze dell'Ingegneria Civile e dell'Architettura, Politecnico di Bari, 70125 Bari, Italy

(Received ?; revised ?; accepted ?. - To be entered by editorial office)

We consider biaxial straining of a dense layer of spheres in a viscous fluid and employ force and moment equilibrium to determine the trajectory of particle pairs that contribute to the stress. In doing this, we use Stokesian Dynamics simulations to guide the choice of the near-contacting pairs that follow such a trajectory. We specify the boundary conditions on the representative trajectory, determine the distribution of particles along it, and how the stress depends on the microstructure and strain-rate. We test the resulting predictions using the numerical simulations. Also, we show that the relation between the tensors of stress and strain rate involves the second and fourth moments of the particle distribution function.

Key words: Authors should not enter keywords on the manuscript, as these must be chosen by the author during the online submission process and will then be added during the typesetting process (see http://journals.cambridge.org/data/relatedlink/jfm-keywords.pdf for the full list)

1. Introduction

In a recent study, Jenkins and La Ragione (2015) determine the typical trajectory of an equilibrated pair of particles of a dense, two-dimensional suspensions of spheres subjected to a simple shearing flow. They evaluate the distribution function of near-contacting neighbors along the trajectory and, using this distribution function and the expression for the force between two equilibrated near-contacting neighbors, they predict the particle pressure, the difference in normal stresses, and the difference between the average rotation of the spheres and half the vorticity of the average velocity.

Here, we focus on biaxial straining of a dense layer of spheres and, as an extension of the previous work, also introduce moment equilibrium. We employ Stokesian Dynamics numerical simulations to guide the choice of the near-contacting pairs on a representative trajectory that contributes most to the inter-particle stress. We specify the boundary conditions on the representative trajectory, determine the distribution of particles along it, and the relationship between stress, microstructure and strain-rate. We test these predictions against the results of the numerical simulations. We show that the relation between the stress and strain rate tensors involves the second and fourth moments of

† Email address for correspondence: jtj2@cornell.edu

the particle distribution, and place this and other aspects of our approach in the context of earlier models that focused on the second moment (Phan-Thien 1995; Stickel, et al. 2006; Goddard, 2006).

The approximate satisfaction of force and moment equilibrium of particles in the flow plays an important role in what we do. In that regard, we operate in the spirit of Nazockdast and Morris (2012a, 2012b, 2013) or that of the statistical characterization by Thomas et. al. (2018) of equilibrated particles sheared in two dimensions, but in the limit of dense flows of the simpler pure shearing flow. The analysis must be extended to three-dimensional rotational shearing flows before it can be placed in relation to phenomenological relations that have resulted from experiments on dense three-dimensional shearing flows (Boyer, et al. 2011; Guazzelli and Pouliquen 2018).

2. Micro-mechanics

A steady, planar, pure shearing flow of a dense suspensions of identical spheres with radius a is characterized by an average rate of deformation tensor $\mathbf{D}$ with nonzero components $D_{11} = -D_{22} = \dot{\gamma}$, where x_1 and x_2 are the axes in the directions of greatest extension and compression, respectively, and $\dot{\gamma}$ is the constant shear rate. We focus on a typical pair of spheres and their near-contacting neighbors, and take $\hat{\mathbf{d}}^{(BA)}$, to be the unit vector directed from the center of sphere A to that of sphere B, with $\hat{\mathbf{d}}^{(AB)} = -\hat{\mathbf{d}}^{(BA)}$. Then, with $\theta^{(BA)}$ the time-dependent angle between $\hat{\mathbf{d}}^{(BA)}$and the x_2 axis,

$$\hat{d}_\alpha^{(BA)} = (\sin\theta^{(BA)}, \cos\theta^{(BA)}) \tag{2.1}$$

and the components of the unit tangent vector, $\hat{\mathbf{t}}^{(BA)} = -\hat{\mathbf{t}}^{(AB)}$, perpendicular to it, are

$$t_\alpha^{(BA)} = (\cos\theta^{(BA)}, -\sin\theta^{(BA)}), \tag{2.2}$$

or $t_\alpha^{(BA)} = \varepsilon_{\alpha\beta} d_\beta^{(BA)}$, where $\varepsilon_{12} = -\varepsilon_{21} = 1$ and $\varepsilon_{11} = \varepsilon_{22} = 0$.

2.1. *Kinematics*

In a pure shearing flow, the relative motion of the center of particle B with respect to the center of particle A is

$$v_\alpha^{(BA)} = \frac{ds^{(BA)}}{dt}\hat{d}_\alpha^{(BA)} + 2a\frac{d\theta}{dt}^{(BA)}\hat{t}_\alpha^{(BA)}, \tag{2.3}$$

where s is the separation of the edges along the line of centers. The relative velocity of their points of near contact is, then,

$$v_\alpha^{(BA)} + a(\omega^{(A)} + \omega^{(B)})\hat{t}_\alpha^{(BA)} \equiv v_\alpha^{(BA)} + aS\hat{t}_\alpha^{(BA)}, \tag{2.4}$$

where ω is the angular velocity of the sphere and S is their sum.

The interaction of A with a near contacting neighbors n, other than B, is treated differently; the sphere n is assumed to move relative to A with the average flow. Then, the relative velocity of centers of pair nA is

$$v_\alpha^{(nA)} = 2aD_{\alpha\beta}\hat{d}_\beta^{(nA)} \tag{2.5}$$

and the relative velocity of the points of near contact nA is

$$v_\alpha^{(nA)} + a\omega^{(A)}\hat{t}_\alpha^{(nA)}. \tag{2.6}$$

2.2. *Force*

The force of interaction between a typical pair BA of particles is related to the relative velocity and distance between their points of near contact. According to Jeffrey and

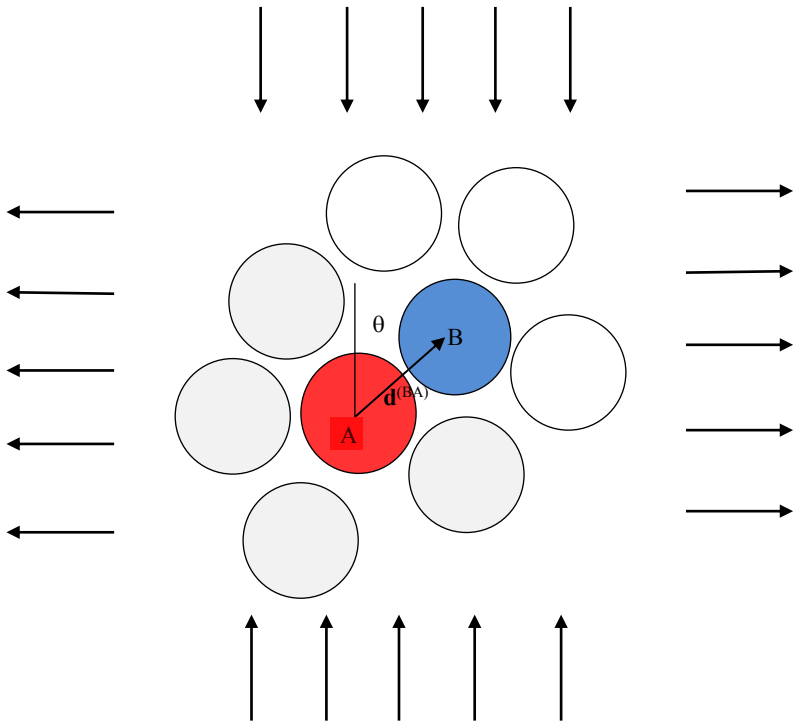

Figure 1: The pair $A - B$ and the near-contacting neighbors of A, showing the angle $\theta^{(BA)}$ and the vector $\mathbf{d}^{(BA}$from the center of A to that of B.

Onishi (1984) and Jeffrey (1992), the force $\mathbf{F}^{(BA)}$ exerted by sphere B on sphere A through a fluid with viscosity μ, is

$$F_\alpha^{(BA)} = 6\pi\mu a K_{\alpha\beta}^{(BA)} v_\beta^{(BA)} - \frac{F_0}{s^{(BA)}} \hat{d}_\alpha^{(BA)} - 9.54\pi\mu a^2 \left(\hat{t}_\beta D_{\beta\xi} \hat{d}_\xi\right) \hat{t}_\alpha^{(BA)} \\ + \pi\mu a^2 \left[\ln\left(\frac{a}{s^{(BA)}}\right) - 0.96\right] \omega^{(A)} \hat{t}_\alpha^{(BA)} + \pi\mu a^2 \ln\left(\frac{a}{s^{(BA)}}\right) \omega^{(B)} \hat{t}_\alpha^{(BA)}, \tag{2.7}$$

where

$$K_{\alpha\beta}^{(BA)} = \frac{1}{4} \frac{a}{s^{(BA)}} \hat{d}_\alpha^{(BA)} \hat{d}_\beta^{(BA)} + \left[\frac{1}{6} \ln\left(\frac{a}{s^{(BA)}}\right) + 0.64\right] \hat{t}_a^{(BA)} \hat{t}_\beta^{(BA)} \tag{2.8}$$

and the constant terms have been retained because they are the same order as the logarithms. The interaction force also includes a short-range repulsive force of strength F_0 (e.g. Singh and Nott, 2000).

We take the near-contacting neighbors, $n \neq B$, to be those that most influence equilibrium and make the greatest contribution to the stress. There are k-1 of these per sphere and we assume that the separation between their edges is $\bar{s}$. The number of near-contacting neighbors is expected to be less, perhaps far less, that the number of nearest neighbors.

For the near-contacting neighbors, the corresponding force is based on the average motion and the separation $\bar{s}$:

$$F_\alpha^{(nA)} = \frac{3}{\bar{s}} a^2 \pi\mu \left(D_{\beta\xi} \hat{d}_\xi^{(nA)} \hat{d}_\beta^{(nA)} \right) \hat{d}_\alpha^{(nA)} + \pi\mu a^2 \left[\ln\left(\frac{a}{\bar{s}}\right) - 0.96 \right] \omega^{(A)} \hat{t}_\alpha^{(nA)} + 2a^2 \pi\mu \left[\ln\left(\frac{1}{\bar{s}}\right) - 0.96 \right] \left(D_{\beta\xi} \hat{t}_\xi^{(nA)} \hat{d}_\beta^{(nA)} \right) \hat{t}_\alpha^{(nA)} - \frac{F_0}{\bar{s}} \hat{d}_\alpha^{(nA)}. \tag{2.9}$$

2.3. *Equilibrium*

As do Jenkins and La Ragione (2015), we require the equilibrium of a typical pair of spheres under the action of their near-contacting neighbors. However, while they employ only force equilibrium, here we consider the equilibrium of both force and moment. The focus on a flow in which there is no average rotation makes this easier to do; and the possibility of solving for both the translational and rotational degrees of freedom of a typical pair should increase the accuracy of the modeling.

Force equilibrium for particle A is

$$F_\alpha^{(BA)} + \sum_{n \neq B}^{N^{(A)}} F_\alpha^{(nA)} = 0; \tag{2.10}$$

and that for particle B is

$$F_\alpha^{(AB)} + \sum_{m \neq A}^{N^{(B)}} F_\alpha^{(mB)} = 0, \tag{2.11}$$

with $F_\alpha^{(BA)} = -F_\alpha^{(AB)}$. The difference in the force balances projected along $\hat{\mathbf{d}}^{(BA)}$ is

$$3\pi\mu a \frac{a}{s^{(BA)}} \frac{ds^{(BA)}}{dt} - 2\frac{F_0}{s^{(BA)}} + 6\pi\mu a^2 \frac{a}{\bar{s}} \hat{d}_\alpha^{(BA)} J_{\alpha\beta\gamma} D_{\beta\gamma} - 2\frac{F_0}{\bar{s}} Y_\alpha \hat{d}_\alpha^{(BA)} = 0; \tag{2.12}$$

while along $\hat{t}_\alpha^{(BA)}$ is

$$0 = 4\left[\ln\left(\frac{a}{s^{(BA)}}\right) + 3.84 \right] \frac{d\theta^{(BA)}}{dt} - 19 \hat{t}_\beta^{(BA)} D_{\beta\xi} \hat{d}_\xi^{(BA)} + \left[2\ln\left(\frac{a}{s^{(BA)}}\right) - 0.96 \right] S + \left[\ln\left(\frac{a}{\bar{s}}\right) - 0.96 \right] S \varepsilon_{\alpha\beta} Y_\beta^{(BA)} t_\alpha^{(BA)} + 6\frac{1}{\bar{s}} D_{\beta\xi} J_{\alpha\xi\beta}^{(BA)} t_\alpha^{(BA)} + 2\left[2\ln\left(\frac{1}{\bar{s}}\right) - 1.92 \right] D_{\beta\xi} J_{\alpha\xi\beta}^{(BA)} t_\alpha^{(BA)}, \tag{2.13}$$

with

$$J_{\alpha\xi\beta}^{(BA)} = \sum_{n \neq B}^{N^{(A)}} \hat{d}_\alpha^{(nA)} \hat{d}_\beta^{(nA)} \hat{d}_\xi^{(nA)} \tag{2.14}$$

and

$$Y_\alpha^{(BA)} = \sum_{n \neq B}^{N^{(A)}} \hat{d}_\alpha^{(nA)}. \tag{2.15}$$

In writing Eqs.(2.12) and (2.13), we assume that $J^{(BA)}_{\alpha\xi\beta} = -J^{(AB)}_{\alpha\xi\beta}$ and $Y^{(BA)}_{\alpha} = -Y^{(AB)}_{\alpha}$; that is, the arrangement of near-contacting neighbors of B is the reflection of that of A. The terms proportional to S incorporate the influence of the rotations on force equilibrium.

Moment equilibrium for particle A is

$$\varepsilon_{\alpha\beta} d^{(BA)}_{\alpha} F^{(BA)}_{\beta} + \varepsilon_{\alpha\beta} \sum_{n\neq B}^{N^{(A)}} d^{(nA)}_{\alpha} F^{(nA)}_{\beta} = 0, \tag{2.16}$$

and that for particle B is

$$\varepsilon_{\alpha\beta} d^{(AB)}_{\alpha} F^{(AB)}_{\beta} + \varepsilon_{\alpha\beta} \sum_{m\neq A}^{N^{(B)}} d^{(mB)}_{\alpha} F^{(mB)}_{\beta} = 0; \tag{2.17}$$

so their sum is

$$\begin{aligned} 0 = {} & 4\left[\ln\left(\frac{a}{s^{(BA)}}\right) + 3.84\right]\frac{d\theta^{(BA)}}{dt} - 19\hat{t}^{(BA)}_{\mu} D_{\mu\xi} \hat{d}^{(BA)}_{\xi} \\ & + \left[2\ln\left(\frac{a}{s^{(BA)}}\right) - 0.96\right] S + \left[\ln\left(\frac{a}{\bar{s}}\right) - 0.96\right] S\,(k-1) \\ & + 2\left[2\ln\left(\frac{1}{\bar{s}}\right) - 1.92\right] \varepsilon_{\xi\nu} A^{(BA)}_{\nu\mu} D_{\mu\xi}, \end{aligned} \tag{2.18}$$

with

$$A^{(BA)}_{\nu\mu} = \sum_{n\neq B}^{N^{(A)}} \hat{d}^{(nA)}_{\nu} \hat{d}^{(nA)}_{\mu} \tag{2.19}$$

and, again, $A^{(BA)}_{\nu\mu} = A^{(AB)}_{\nu\mu}$.

The tensors $\mathbf{A}$, $\mathbf{J}$ and $\mathbf{Y}$ provide information about the distribution of spheres about a typical pair A-B. We assume here that the distributions about a pair at a given orientation is the average over all pairs at that orientation. These average distributions should depend on both $\hat{\mathbf{d}}^{(AB)}$ and $\mathbf{D}$. As do Jenkins and La Ragione (2015), we treat the local equilibrium with the approximation that $\mathbf{A}$, $\mathbf{J}$ and $\mathbf{Y}$ are independent of $\mathbf{D}$. Then,

$$A^{(BA)}_{\nu\mu} = b_1 \delta_{\nu\mu} + b_2 \hat{d}^{(BA)}_{\mu} \hat{d}^{(BA)}_{\nu}, \tag{2.20}$$

$$J^{(BA)}_{\alpha\xi\beta} = b_3 \hat{d}^{(BA)}_{\alpha} \hat{d}^{(BA)}_{\xi} \hat{d}^{(BA)}_{\beta} + b_4 \left(\hat{d}^{(BA)}_{\alpha} \delta_{\xi\beta} + \hat{d}^{(BA)}_{\xi} \delta_{\alpha\beta} + \hat{d}^{(BA)}_{\beta} \delta_{\xi\alpha}\right), \tag{2.21}$$

and

$$Y^{(BA)}_{\alpha} = b_5 \hat{d}^{(BA)}_{\alpha} \tag{2.22}$$

To calculate the coefficients, Jenkins and La Ragione (2015) assume that given sphere B, the remaining near-contacting neighbors of A spheres are distributed uniformly around its circumference. The results are given as a function of coordination number k through

$$b = -\frac{3\sqrt{3}\,(k-1)}{16\pi}, \tag{2.23}$$

by

$$b_1 = \frac{k-1}{2} - b,\ b_2 = 2b,\ b_3 = 0, \text{and } b_4 = b,\ b_5 = 4b. \tag{2.24}$$

In the pure straining flow of interest,

$$\hat{t}^{(BA)}_{\mu} D_{\mu\xi} \hat{d}^{(BA)}_{\xi} = \dot{\gamma} \sin 2\theta \quad \text{and} \quad \hat{d}^{(BA)}_{\mu} D_{\mu\xi} \hat{d}^{(BA)}_{\xi} = -\dot{\gamma} \cos 2\theta. \tag{2.25}$$

We use these in the differences of the components of the force balances, make lengths dimensionless by the sphere radius a, time by the inverse of the shear rate, forces by $\pi a^3\mu\dot{\gamma}$, write the dimensionless repulsive force as $\hat{F} = F_0/(\pi a^3\mu\dot{\gamma})$, and remove the superscript (BA). Then, the normal component becomes

$$\frac{1}{s}\frac{ds}{d\gamma} = \frac{2}{3}\hat{F}\left(\frac{1}{s}+\frac{4b}{\bar{s}}\right)+\frac{4b}{\bar{s}}\cos 2\theta; \tag{2.26}$$

and the tangential component is

$$\left[\ln\left(\frac{1}{s}\right)+3.84\right]\frac{d\theta}{d\gamma} = \left[c_1+c_2\ln\left(\frac{1}{s}\right)\right]\sin 2\theta, \tag{2.27}$$

with

$$c_1 = 4.77-3\frac{b}{\bar{s}} \text{ and } c_2 = \frac{6b/\left[\bar{s}\left(4b-k+1\right)\right]}{\ln\left(1/\bar{s}\right)-0.96}. \tag{2.28}$$

and we have employed the difference in force balance and the sum of moment equilibrium to write

$$S = -2c_2\sin 2\theta. \tag{2.29}$$

The balances of force and moment, Eqs.(2.26) , (2.27), and (2.29), employed in Eq. (2.7) , provide an expression for $\mathbf{F}^{(BA)}$ in terms of average quantities:

$$\begin{aligned} F_\alpha^{(BA)} = {} & 4b\frac{F_0}{\bar{s}}\hat{d}_\alpha^{(BA)}+\pi\mu a^3\frac{6b}{\bar{s}}\cos 2\theta\dot{\gamma}\hat{d}_\alpha^{(BA)}+\pi\mu a^2\left(2c_1+0.96c_2\right)\sin 2\theta\dot{\gamma}\hat{t}_a^{(BA)} \\ & -9.54\pi\mu a^2\sin 2\theta\dot{\gamma}\hat{t}_\alpha^{(BA)}. \end{aligned} \tag{2.30}$$

This is later employed in the calculation of the stress

2.4. *Representative trajectory*

We identify the representative trajectory as that which particle B traverses with respect to particle A in a succession of equilibrated states, while the other near-contacting particles, n, of the pair move with the average flow, at the constant distance $\bar{s}$ from the pair. The equation that determines this trajectory results from force and moment equilibrium and is a function of two parameters: the average number of near-contacting particles, k, and the average distance, $\bar{s}$. Upon combining Eqs.(2.26) and (2.27), it is

$$\frac{ds}{d\theta} = \frac{2}{3\bar{s}}\frac{\hat{F}\left(\bar{s}+4bs\right)+6bs\cos 2\theta}{\left[c_1+c_2\ln\left(1/s\right)\right]\sin 2\theta}\left[\ln\left(\frac{1}{s}\right)+3.84\right]. \tag{2.31}$$

The trajectory begins at θ_0 and ends at θ_1, and both angles must be determined. Because of the presence of $\hat{F}$, the trajectory is asymmetric about $\pi/4$, and θ_0 differs from $\pi/2-\theta_1$.

The amount of total strain, $\hat{\gamma}$, necessary to complete the trajectory may be calculated from the pair interaction in the average flow. From Eq.(2.27)

$$\frac{d\gamma}{d\theta} = \frac{\ln\left(1/s\right)+3.84}{\left[c_1+c_2\ln\left(1/s\right)\right]\sin 2\theta}; \tag{2.32}$$

so,

$$\hat{\gamma} = \int_{\theta_0}^{\theta_1}\frac{\ln\left(1/s\right)+3.84}{\left[c_1+c_2\ln\left(1/s\right)\right]\sin 2\theta}d\theta. \tag{2.33}$$

2.5. *Particle distribution*

We next introduce the distribution of near-contacting neighbors along the trajectory, $A(\theta)$, defined so that $A\left(\theta\right)d\theta$ is the average number of such particles within the element $d\theta$. At steady state, the flux, $A\left(\theta\right)d\theta/d\gamma$, of these equilibrated particles along the

trajectory is constant. That is, particles are more likely to be where the velocity along the trajectory is least. Because the repulsive force breaks the symmetry of approach and departure, the distribution is anticipated to be asymmetric about $\pi/4$. In computations, we implement the flux condition as a differential equation

$$\frac{dA}{d\theta} = -\frac{A}{\dot{\theta}}\frac{d\dot{\theta}}{d\theta}, \tag{2.34}$$

with

$$\frac{d\dot{\theta}}{d\theta} = \frac{\partial\dot{\theta}}{\partial\theta} + \frac{\partial\dot{\theta}}{\partial s}\frac{ds}{d\theta}. \tag{2.35}$$

The distribution $A(\theta)$ is related to the average number near-contacting neighbors per particle by

$$4\int_{\theta_0}^{\theta_1} A(\theta)\, d\theta = k. \tag{2.36}$$

We implement this as a differential equation for the partial number of near-contacting neighbors

$$I(\theta) \equiv \int_{\theta_0}^{\theta} A(\theta')\, d\theta', \tag{2.37}$$

as

$$\frac{dI}{d\theta} = A(\theta), \tag{2.38}$$

with boundary conditions $I(\theta_0) = 0$ and $I(\theta_1) = k/4$.

Given that the beginning and ending angles of the trajectory differ, we take the beginning and ending values of the particle separation to be the same. There are three first-order differential equations, Eqs. (2.31), (2.34), and (2.38), for s, A, and I as functions of θ, and four boundary conditions: one for each of s_0 and s_1 that introduce a single parameter, and two for I. Consequently, θ_1 may be determined as part of the solution. The inputs are θ_0, $s_0 = s_1$, $\bar{s}$, and k In Appendix B, we provide the Matlab code that is employed in the solver. We generate solutions and compare them with the results of Stokesian Dynamics simulations in a later section.

3. Particle stress

Knowledge of the distribution of near-contacting neighbors $A(\theta)$ and the contact forces along the trajectory permits the calculation of the macroscopic particle stress in the suspension. The stress tensor is, according to Cauchy (Love 1944, Appendix, Note B),

$$T_{\alpha\beta} = na\int_0^{2\pi} A(\theta)\, F_\alpha \hat{d}_\beta d\theta, \tag{3.1}$$

with F_α given by its equilibrium expression, Eq.(2.30). The dimensionless form of this, $t_{a\beta} = T_{\alpha\beta}/(2a\mu\dot{\gamma})$ with $n = \nu/(\pi a^2)$, is

$$\begin{aligned} t_{a\beta} = \nu\frac{b}{\bar{s}}\int_0^{2\pi} A(\theta)\left(2\hat{F} + 3\cos 2\theta\right)\hat{d}_\alpha\hat{d}_\beta d\theta \\ +\nu\left(c_1 + 0.48c_2 - 4.77\right)\int_0^{2\pi} A(\theta)\sin 2\theta\hat{t}_a\hat{d}_\beta d\theta. \end{aligned} \tag{3.2}$$

The particle shear stress,

$$\tau \equiv \frac{1}{2}\left(t_{11}-t_{22}\right), \tag{3.3}$$

is

$$\tau = -2\nu\frac{b}{\bar{s}}\int_0^{\pi/2} A\left(\theta\right)\left(2\hat{F}+3\cos 2\theta\right)\cos 2\theta d\theta \\ +\nu\left(2c_1+0.96c_2-9.54\right)\int_0^{\pi/2} A\left(\theta\right)\sin^2 2\theta d\theta, \tag{3.4}$$

where, we recall, that

$$b = -\frac{3\sqrt{3}\left(k-1\right)}{16\pi}, \tag{3.5}$$

$$c_1 = 4.77 - 3\frac{b}{\bar{s}}, \text{ and } c_2 = \frac{6b/\left[\bar{s}\left(4b-k+1\right)\right]}{\ln\left(1/\bar{s}\right)-0.96}. \tag{3.6}$$

This shear stress depends on the separation, $\bar{s}$, of near-contacting neighbors other than B, and on the area fraction, explicitly and through the coordination number, k. Because the direct contribution of the repulsive force to the integral is very small and the trigonometric factors associated with the other contributions are even about $\pi/4$, the shear stress is independent of the asymmetry of the particle distribution about $\pi/4$. In contrast, this asymmetry is crucial to the determination of the pressure; the important influence of the repulsive force enters in creating it.

The particle pressure,

$$p \equiv -\frac{1}{2}\left(t_{11}+t_{22}\right), \tag{3.7}$$

is

$$p = -2\nu\frac{b}{\bar{s}}\int_0^{\pi/2} A\left(\theta\right)\left(2\hat{F}+3\cos 2\theta\right)d\theta. \tag{3.8}$$

This pressure also depends on $\bar{s}$ and ν and its existence is due to the asymmetry of A about $\pi/4$. This asymmetry is due to that of the separation along the representative trajectory created by $\hat{F}$ and the influence of the asymmetry of the separation on the angular velocity, $\dot{\theta}$. The particle pressure and the mechanisms responsible for it are a focus of this paper; a particle shear stress may be calculated based on the average flow, although that determined here is several time less than this because of the approximate satisfaction of equilibrium.

Particle stresses associated with motion along the representative trajectories are compared with those measured in Stokesian Dynamics simulations after a discussion of the simulations.

4. Stokesian Dynamics

We determine the trajectories of spherical particles in the flows by performing simulation with the same conditions as the theory (a monolayer with no inertia). We impose a fixed flow profile of planar extensional flow, so-called pure shear, with shear rate $\dot{\gamma}$ ($\dot{\varepsilon}$ is used in Seto et al., 2017):

$$\boldsymbol{u}^{\infty}(\boldsymbol{r}) = \mathbf{D}\cdot\boldsymbol{r}, \quad \mathbf{D} = \begin{pmatrix}\dot{\gamma} & 0\\ 0 & -\dot{\gamma}\end{pmatrix}. \tag{4.1}$$

A simulation box with periodic boundary conditions constantly deforms according to this. Significant deformations of the simulation box can be avoided by using the Kraynik -Reinelt periodic boundary conditions, which take the deformed box to the original square box after a constant strain interval (Kraynik and Reinelt 1992, Todd and Daivis, 1998, Seto et al., 2017). Thus, the flow can be maintained for a sufficiently long time to evaluate its steady states.

Due to the negligible inertia of the particles, translational and angular velocities can be determined by solving the force and torque balance equations for the respective particles ($i = 1, \ldots, N$):

$$\begin{pmatrix} \mathbf{0} \\ \mathbf{0} \end{pmatrix} = \begin{pmatrix} \boldsymbol{F}_{\mathrm{H}} \\ \boldsymbol{T}_{\mathrm{H}} \end{pmatrix} + \begin{pmatrix} \boldsymbol{F}_{\mathrm{R}} \\ \mathbf{0} \end{pmatrix}. \tag{4.2}$$

Here, a vector, such as $\boldsymbol{F}_{\mathrm{H}}$, represent all N particles, $\boldsymbol{F}_{\mathrm{H}} \equiv (\boldsymbol{F}_{\mathrm{H}}^{(1)}, \ldots, \boldsymbol{F}_{\mathrm{H}}^{(N)})$.

The hydrodynamic interactions in the Stokes, zero Reynolds number, regime are linear in the velocities:

$$\begin{pmatrix} \boldsymbol{F}_{\mathrm{H}} \\ \boldsymbol{T}_{\mathrm{H}} \end{pmatrix} = -\mathbf{R}_{\mathrm{FU}} \cdot \begin{pmatrix} \boldsymbol{U} - \boldsymbol{u}^{\infty} \\ \boldsymbol{\Omega} \end{pmatrix} + \mathbf{R}_{\mathrm{FE}} : \mathbf{D}_{\mathrm{N}}. \tag{4.3}$$

There exist several levels of approximations to construct the resistance matrices $\mathbf{R}_{\mathrm{FU}}$ and $\mathbf{R}_{\mathrm{FD}}$. Brady and Bossis (1988) constructed them using truncated multipole expansions for the far-field interactions and a pair-wise solution for lubrication interactions. In this work, we focus on a special situation in which repulsive forces are very weak in comparison with viscous drag forces. Under such conditions, particles tend to approach their neighbors very closely. Because the resistance coefficients diverge at contacts ($s = 0$), the nearly touching hydrodynamic interactions dominate the dynamics. This is why we construct the approximate resistance matrices with the leading $1/s$ term in the normal component and the logarithmic term $\log(1/s)$ and following constants in the tangential component, using the solution for two nearly-touching rigid spheres (Jeffrey and Onishi, 1984, Jeffrey, 1992). (A detailed descriptions can be seen elsewhere, c.f. Mari el al., 2014.) The hydrodynamic interaction is effective until a cutoff distance, $s < 0.10$; thus, the resistance coefficients remain positive in this range.

The repulsive force employed in this work is the same as that used in Nott and Brady (1994).

$$\boldsymbol{F}_{\mathrm{R}} = F_0 \frac{\sigma e^{-\sigma s}}{1 - e^{-\sigma s}} \boldsymbol{n} \approx \frac{F_0}{s} \boldsymbol{n}. \tag{4.4}$$

Here, we investigate a very weak repulsive force, $F_0 = 10^{-4}$. Because the repulsive force diverges in the limit of contact, $s \to 0$, and this divergence is much stronger than that of the resistance coefficients, the gap, s, remains positive. Therefore, contact forces do not appear in the current system.

By solving the force and torque balance equations (4.2) with the hydrodynamic iteration (4.3) and repulsive force (4.4), the linear and angular velocities $(\boldsymbol{U}, \boldsymbol{\Omega})$ can be determined at each time step. Integrating these velocities $\boldsymbol{U} = (\boldsymbol{U}^{(1)}, \ldots, \boldsymbol{U}^{(N)})$ with a discretized time step, we obtain trajectories of respective particles. The particle stress tensor $\boldsymbol{T}$ is given by the symmeterized first moment:

$$\boldsymbol{T} = \frac{1}{V} \sum_j \frac{(\boldsymbol{r}^i - \boldsymbol{r}^j)\boldsymbol{F}^{ij} + (\boldsymbol{r}^j - \boldsymbol{r}^i)\boldsymbol{F}^{ji}}{2}, \tag{4.5}$$

with the pairwise forces, $\boldsymbol{F}^{ij} \equiv \boldsymbol{F}_{\mathrm{Lub}}^{ij} + \boldsymbol{F}_{\mathrm{R}}^{ij}$ and positions r^{ij} and r^{ji} of all interacting particle pairs. We omit the stress contribution from the fluid. Here, $V = 2aL^2$ is the vol-

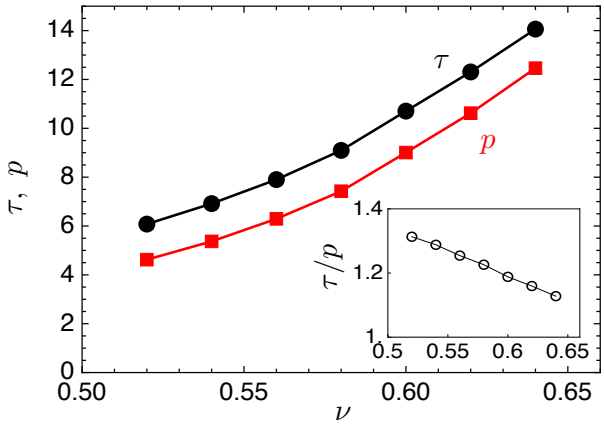

Figure 2: Shear stress τ and pressure p.

ume of the monolayer system. Normalizing the symmeterized first moment with the shear stress of the suspending fluid $2\mu\dot{\gamma}$, gives the dimensionless stress $t_{\alpha\beta} \equiv T_{\alpha\beta}/2\mu\dot{\gamma}$. Thus, we have the dimensionless particle pressure $p \equiv -(t_{11} + t_{22})/2$ and the dimensionless particle shear stress $\tau \equiv (t_{11} - t_{22})/2$, respectively.

5. Simulation results

We simulate monolayer systems with 1000 spheres of radius a at area fractions ν between 0.52 and 0.64. We generate initial configurations with a simple algorithm using random numbers. To reduce effects of such artificially generated initial configurations, the post-processing analyses use steady states data from 10 to 50 strain units.

Fig. 2 shows the area fraction ν dependences of the shear stress τ and pressure p. They increase in a similar manner with ν, but the ratio τ/p decreases gradually. Most of stress is generated by closely approaching particles. We define the near-contacting particles as those with a separation less than one percent of the particle radius. As seen in Fig. 3, more than 90% of shear stress is generated from particle pairs with $0 < s < 0.01$. Moreover, such near-contacting particles generates almost 100% of the pressure p.

We can check the concentration of stress contribution in the very narrow range of s using distribution maps. We calculate the spatial distribution in $\xi \equiv \log s$. The statistics are calculated with discretized bins $\xi_k \equiv \xi_1 + (k-1)\Delta\xi$, $k = 1, \ldots, k_{\max}$. $\xi_1 = \log 10^{-7}$ and $\xi_{k_{\max}} = \log 10^{-1}$. The results are plotted with s in a logarithmic scale. Fig. 4(a) displays the probability distribution $P(s, \theta)$ of the same simulation, indicating that particles tend to remain near the stagnation point $(\theta, s) \approx (0, 10^{-6})$. The hot-spot band spreads until $\theta \sim \pi/4$. We also separately calculate the stress of (4.5) constructed with normal forces $\boldsymbol{F}^{ij}_{\rm n} \equiv \boldsymbol{F}^{ij} \cdot \boldsymbol{n}^{ij}\boldsymbol{n}^{ij}$ and tangential forces $\boldsymbol{F}^{ij}_{\rm t} \equiv \boldsymbol{F}^{ij} - \boldsymbol{F}^{ij} \cdot \boldsymbol{n}^{ij}\boldsymbol{n}^{ij}$. As shown in Fig. 3(b), 80 % of shear stress τ indeed comes from the normal forces.

Besides systematic motions due to the shearing deformation, particle motions fluctuate due to occasional configurations of surrounding particles. Therefore, it is necessary to reconstruct averaged trajectories to compare with theoretical ones. To this end, we first calculate the averaged relative-velocity field $\langle \boldsymbol{U}^{(j)} - \boldsymbol{U}^{(i)} \rangle$ over all interacting pairs i and j in terms of the relative position coordinate $\Delta\boldsymbol{r}^{ij} = (2a + s, \theta)$. Owing to the symmetry of pure shear, the statistics are taken on a quadrant: $0 < \theta < \pi/2$. Because we consider a situation that is very close to the singularity (Ball and Melrose 1995), the particles tend to approach very close to contact i.e., a bundle of trajectories is compressed into

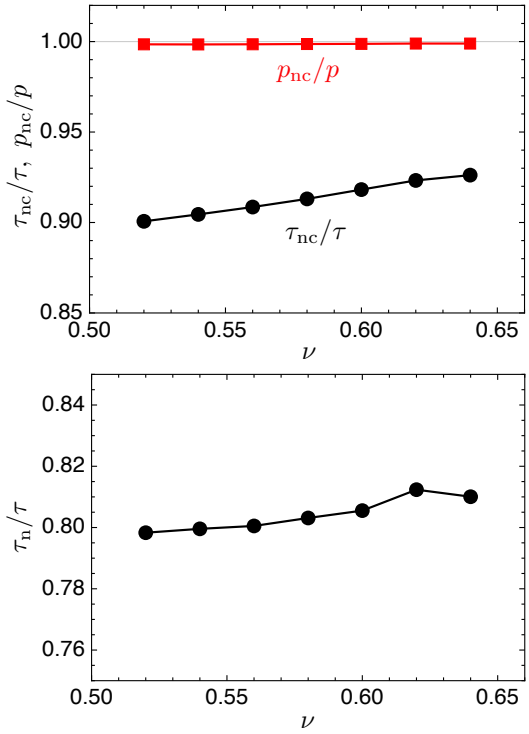

Figure 3: (a) Near-contact contributions to τ and p. (b) Approximately 80 % of the shear stress τ comes from the normal force. The partial stress is obtained using only the normal component of the pairwise force in (4.5).

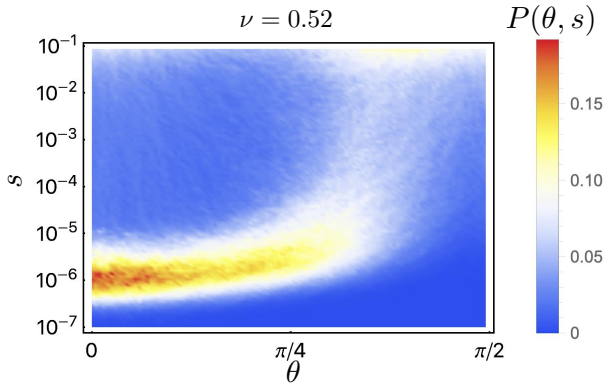

Figure 4: Probability distribution. The s axis is logarithmic.

an extremely narrow range of s. To avoid a loss of precision due to averaging, we carry out the statistical data binning in a logarithmic scale of s. Once we evaluate the velocity field in the $(\log s, \theta)$ space, i.e., $(\langle \dot{s}/s \rangle, \langle \dot{\theta} \rangle)$, we can obtain trajectories as streamlines of the velocity field. In Fig. 5, trajectories of the system with $\nu = 0.52$ and initial positions: $(\theta_0, s_0) = (q\pi/96, 0.09)$ $(q = 1, \ldots, 24)$. are plotted using a logarithmic scale for s.

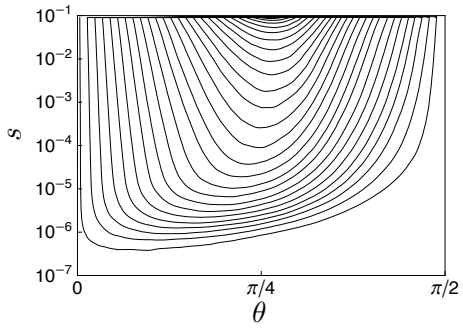

Figure 5: Trajectories reconstructed from the averaged velocity field at $\nu = 0.52$, with a logarithimic scale for s.

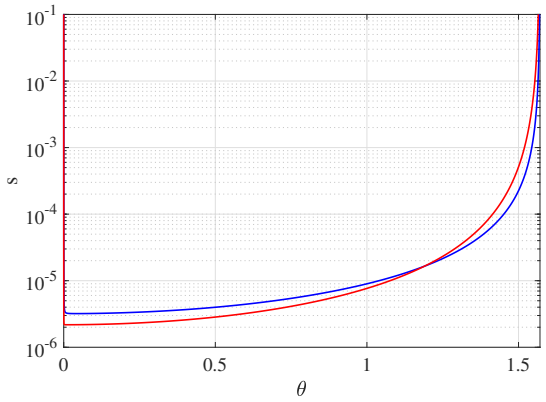

Figure 6: The logarithm of the separation along the trajectory, for $\nu = 0.52$, $k = 2.01$ (blue) and $\nu = 0.64$, $k = 2.48$ (red), with $\theta_0 = 10^{-6}$, $F = 10^{-4}$, and $\bar{s} = 0.02$.

6. Model predictions

We take $\theta_0 = 10^{-6}$, $s_0 = s_1 = 0.10$, $\bar{s} = 0.02$, and assume that k varies linearly with ν from 2.0, at $\nu = 0.52$, to 2.5, at $\nu = 0.64$. These values and the relation for k are plausible; they are influenced by the Stokesian Dynamics simulations. A separation $\bar{s}$ of 0.02 gives a shear stress that is close to that measured. This separation is somewhat greater than the width, 0.01, of the interval of particle separation in the Stokesian Dynamics simulations from which 90% to the shear stress and 100% to the pressure is obtained.

Figure 7 shows the logarithm of the separation along the trajectory for $\nu = 0.52$ and $\nu = 0.64$. Figure 8 shows the logarithm of the distribution of near-contacting neighbors along the trajectory. The figures indicate the role played by the repulsive force in creating an asymmetry between approach and departure with increases in area fraction, and its influence on the distribution of particles along the trajectory.

In figures 8 and 9, we plot p and τ. The particle pressure exists because of the asymmetry of approach and departure in the trajectory associated with F. Moreover, given Eq. (2.30), we can identify the normal and tangential component of the force, respectively, along $\hat{\mathbf{d}}^{(\mathbf{BA})}$ and $\mathbf{t}^{(\mathbf{BA})}$. Then the stress, seen as first moment of the force, can be partitioned in a part contributed by the normal component of the viscous forces and in complementary part contributed by the tangential component of the viscous force. Clearly, particle pressure depends only upon the contribution of the normal forces; less

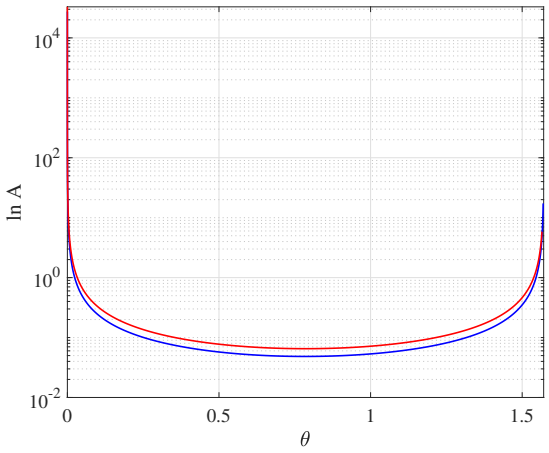

Figure 7: The logarithm of the distribution of near-contacting neighbors along the trajectory, for the parameter values of figure 2. For $\nu = 0.52$, $A(\theta_0) = 2.74\text{x}10^4$ and $A(\theta_1) = 17.29$; for $\nu = 0.64$, $A(\theta_0) = 3.30\text{x}10^4$ and $A(\theta_1) = 5.85$.

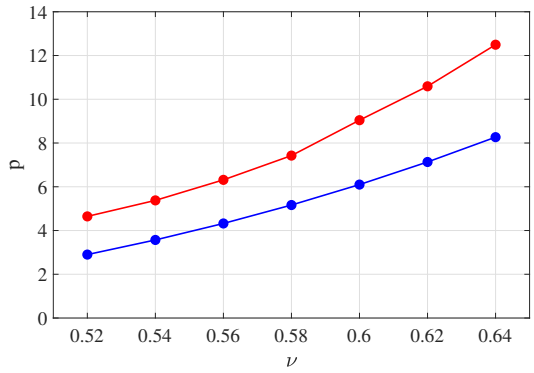

Figure 8: Particle pressure for different area fractions (blue), with $\theta_0 = 10^{-6}$, $F = 10^{-4}$, and $\bar{s} = 0.02$. That measured in Stokesian Dynamics simulations (red).

obvious is the fact that also the shear stress depends almost entirely on the contribution to the stress associated with the normal forces. This is because the greatest contribution to the stress is where particles have the highest concentration, close to $\theta = 0$; here, tangential forces are almost zero and the normal forces are greater.

The predicted particle pressure is somewhat less than that measured in the numerical simulations and the predicted shear stress is somewhat greater. The ratio of shear stress to pressure decreases with area fraction, as in the numerical simulations; but, because of under- and over-predicting, we have a greater value for the ratio.

The model employs approximate satisfaction of force and moment equilibrium. These make it possible to understand the mechanisms that are responsible for the normal and tangential components of the relative velocity of a typical pair of particles. These features include the relationship between the asymmetry of the particle distribution and the repulsive force, and the relative contributions of the normal and tangential viscous forces to the stresses.

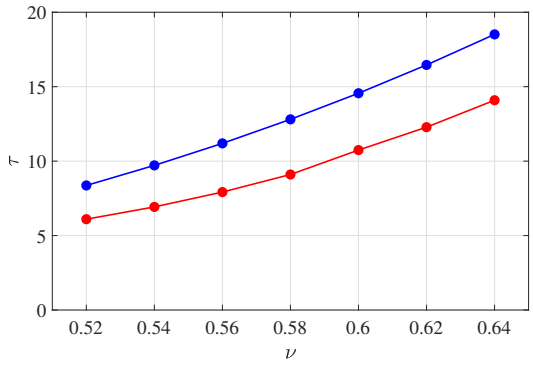

Figure 9: Shear stress for different area fractions (blue), for the parameters of figure 4 That measured in Stokesian Dynamics simulations (red).

7. Tensorial formulation

As elaborated upon by Onat and Leckie (1988) and Advani and Tucker (1987,1990), the distribution of near-contacting neighbors can be represented by an infinite series with respect to basis functions, such as

$$f_{\alpha\beta} = \hat{d}_\alpha \hat{d}_\beta - \frac{1}{2}\delta_{\alpha\beta} \tag{7.1}$$

and

$$g_{\xi\eta\rho\beta} = \hat{d}_\xi \hat{d}_\eta \hat{d}_\rho \hat{d}_\beta - \frac{1}{6}\left(\delta_{\xi\eta}\hat{d}_\rho\hat{d}_\beta + \hat{d}_\xi\hat{d}_\eta\delta_{\rho\beta} + \hat{d}_\xi\hat{d}_\rho\delta_{\eta\beta} + \hat{d}_\eta\hat{d}_\beta\delta_{\xi\rho} + \delta_{\xi\beta}\hat{d}_\eta\hat{d}_\rho + \hat{d}_\xi\hat{d}_\beta\delta_{\eta\rho}\right) + \frac{1}{24}\left(\delta_{\xi\eta}\delta_{\rho\beta} + \delta_{\xi\rho}\delta_{\eta\beta} + \delta_{\xi\beta}\delta_{\eta\rho}\right) : \tag{7.2}$$

$$A(\theta) = \frac{k}{2\pi}\left(1 + 4\mathcal{Z}_{\alpha\beta}f_{\alpha\beta} + 16\mathcal{B}_{\xi\eta\rho\beta}g_{\xi\eta\rho\beta} + ...\right). \tag{7.3}$$

The coefficients $\boldsymbol{\mathcal{Z}}$ and $\boldsymbol{\mathcal{B}}$ are completely traceless and completely symmetric tensors, related to the distribution through

$$\mathcal{Z}_{\alpha\beta} = \int_0^{2\pi} A(\theta) f_{\alpha\beta} d\theta \tag{7.4}$$

and

$$\mathcal{B}_{\xi\eta\rho\beta} = \int_0^{2\pi} A(\theta) g_{\xi\eta\rho\beta} d\theta. \tag{7.5}$$

These are the second and fourth moments of the distribution, respectively.

The stress of Eq.3.1) may be written in terms of these as

$$\begin{aligned} T_{\alpha\beta} = {} & 4nak\frac{F_0}{\bar{s}}b\delta_{a\beta} - n\pi\mu a^3\left(M+N\right)\mathcal{B}_{\alpha\beta\gamma\eta}D_{\gamma\eta} \\ & -n\pi\mu a^3\left(M-N\right)\frac{k}{4}\delta_{\alpha\eta}\delta_{\beta\gamma}D_{\gamma\eta} \\ & -n\pi\mu a^3\left(M+N\right)\frac{1}{6}\delta_{\alpha\beta}\mathcal{Z}_{\eta\gamma}D_{\gamma\eta} \\ & -n\pi\mu a^3\frac{2M-N}{6}\left(\delta_{\alpha\eta}\mathcal{Z}_{\gamma\beta} + \delta_{\beta\eta}\mathcal{Z}_{\gamma\alpha}\right)D_{\eta\gamma}, \end{aligned} \tag{7.6}$$

where

$$M = \frac{6b}{\bar{s}/a} \quad \text{and} \quad N = 2c_1 + 0.96c_2 - 9.54; \tag{7.7}$$

or, more compactly, as

$$T_{\alpha\beta} = na\left(4kb\frac{F_0}{\bar{s}}\delta_{a\beta} + G_{\alpha\beta\gamma\eta}D_{\gamma\eta}\right), \tag{7.8}$$

where

$$G_{\alpha\beta\gamma\eta} = -n\pi\mu a^3\left[\frac{M-N}{4}k\delta_{\alpha\eta}\delta_{\beta\gamma} + \frac{M+N}{6}\delta_{\alpha\beta}\mathcal{Z}_{\eta\gamma} + \frac{2M-N}{6}\left(\delta_{\alpha\eta}\mathcal{Z}_{\gamma\beta} + \delta_{\beta\eta}\mathcal{Z}_{\gamma\alpha}\right)\right] - n\pi\mu a^3(M+N)\mathcal{B}_{\alpha\beta\gamma\eta}. \tag{7.9}$$

The stress depends only on the second and fourth moments of the distribution, although an approximation of the distribution in terms of these does not provide a good representation of it. With knowledge of the distribution function, it is possible to evaluate the components of the second and fourth moments. In particular, when $F = 0$, the only non-zero components are $\mathcal{B}_{1111} = \mathcal{B}_{2222} = -\mathcal{B}_{1122}$; when $F \neq 0$, then $\mathcal{Z}_{11} = -\mathcal{Z}_{22}$ are also different from zero. For example, when $\nu = 0.64$, $k = 2.50$ and $F = 10^{-4}$, their numerical values are $\mathcal{B}_{1111} = 0.25$ and $\mathcal{Z}_{11} = -0.57$. Then, with Eq. (7.8), the dimensionless particle pressure is

$$p = -\nu\frac{b}{\bar{s}}\left(F - 3\mathcal{Z}_{11}\right) = 8.51 \tag{7.10}$$

With the equilibrium equations, it is possible to characterize the role played by moment equilibrium in determining features of the trajectory and the distribution of particles along it. Ignoring moment equilibrium is equivalent to taking $S = 0$, or $c_2 = 0$ in Eq. (2.27). This has an important influence on $\dot{\theta}$. Then, because both the distribution of near-contacting neighbors and the interval over which it is defined depend upon $\dot{\theta}$, there is a dependence of the stress upon it. For example, when $\nu = 0.64$ and moment equilibrium is ignored, p is 14.81, rather than 8.51. That is, the value of p is affected by moment equilibrium through the distribution. In contrast, τ is 18.60, rather than 18.94 and changes little because it is independent of the shape of the distribution.

In the absence of the knowledge of the distribution function, it is possible to develop evolution equations for the approximate determination of its moments (e.g., Prantil et al., 1993). Phan-Thien (1995) and Stickell,et al. (2006) employ such an equation for the second moment, and break the symmetry of approach and departure by including a term in it that is proportional to $[\mathrm{tr}(\mathbf{D}^2)/2]^{1/2}$. Goddard (2006) introduces a memory integral for the second moment - a representation for the solution to its evolution equation - that breaks this symmetry by incorporating a term proportional to the $\mathbf{D}^2$. Theories of this type produce stress relations that are linear in the strain rate; that is, rate-dependent. In contrast, we employ only a short-range repulsive force that is independent of the shear rate. Consequently, our stress relation contains contributions that are independent of rate.

8. Conclusion

We have considered a plane, pure shearing flow of a dense layer of spheres in a viscous fluid. We assumed that there is a short-range repulsive force between the spheres, in addition to the viscous forces associated with the flow. We focused on pairs of spheres, assumed that their neighbors translate with the average flow, and required that they be

in force and moment equilibrium with each other and their neighbors. We then assumed that the neighborhoods of pairs with the same orientation were equal to the average over that orientation; this permitted us to write equations for the radial and angular velocity of the relative motion of a single pair as they began and ended an interaction, and the orientation of their line of centers with the axis of greatest compression of the flow.

Knowledge of the relative circumferential velocity allowed us to phrase a condition on the particle flux that led to a determination of the distribution of near contacting neighbors along a trajectory that contributes most to the particle stress. Because of the presence of the repulsive force, the trajectory on approach is not the same as that on departure. An integral over the distribution and the inter-particle forces that result from equilibrium gave the particle stress. Because of the lack of symmetry on approach and departure, in addition to a particle deviatoric stress, there is a particle pressure.

9. Appendix A

The equilibium equation for particle A is

$$\begin{aligned}0 = {} & 6\pi\mu a K_{\alpha\beta}^{(BA)} v_\beta^{(BA)} - \frac{F_0}{s^{(BA)}}\hat{d}_\alpha^{(BA)} \; - 9.54\pi\mu a^2 \left(\hat{t}_\beta D_{\beta\xi}\hat{d}_\xi\right)\hat{t}_\alpha^{(BA)} + \pi\mu a^2\left[\ln\left(\frac{a}{s^{(BA)}}\right) - 0.96\right]\omega^{(A)}\hat{t}_\alpha^{(BA)} \\ & + \pi\mu a^2 \ln\left(\frac{a}{s^{(BA)}}\right)\omega^{(B)}\hat{t}_\alpha^{(BA)} + \sum_{n\neq B}^{N^{(A)}}\left\{\frac{3}{\bar{s}}a^2\pi\mu\left(D_{\beta\xi}\hat{d}_\xi^{(nA)}\hat{d}_\beta^{(nA)}\right)\hat{d}_\alpha^{(nA)} + \pi\mu a^2\left[\ln\left(\frac{a}{\bar{s}}\right) - 0.96\right]\omega^{(A)}\hat{t}_\alpha^{(nA)}\right\} \\ & + \sum_{n\neq B}^{N^{(A)}}\left\{2a^2\pi\mu\left[\ln\left(\frac{1}{\bar{s}}\right) - 0.96\right]\left(D_{\beta\xi}\hat{t}_\xi^{(nA)}\hat{d}_\beta^{(nA)}\right)\hat{t}_\alpha^{(nA)} - \frac{F_0}{\bar{s}}\hat{d}_\alpha^{(nA)}\right\}. \end{aligned} \tag{9.1}$$

Similar expression can be written for particle B. The difference between force equilibrium A and B leads to

$$\begin{aligned}0 = {} & 12\pi\mu a K_{\alpha\beta}^{(BA)} v_\beta^{(BA)} - 2\frac{F_0}{s^{(BA)}}\hat{d}_\alpha^{(BA)} \; - 2\times 9.54\pi\mu a^2\left(\hat{t}_\beta^{(BA)} D_{\beta\xi}\hat{d}_\xi^{(BA)}\right)\hat{t}_\alpha^{(BA)} \\ & + a^2\pi\mu\left[2\ln\left(\frac{a}{s^{(BA)}}\right) - 0.96\right]S\hat{t}_\alpha^{(BA)} + a^2\pi\mu\left[\ln\left(\frac{a}{\bar{s}}\right) - 0.96\right]S\varepsilon_{\alpha\beta}Y_\beta^{(BA)} \\ & + 2\frac{3}{\bar{s}}a^2\pi\mu D_{\beta\xi}J_{\alpha\xi\beta}^{(BA)} + 2a^2\pi\mu\left[2\ln\left(\frac{1}{\bar{s}}\right) - 1.92\right]D_{\beta\xi}J_{\alpha\xi\beta}^{(BA)} - 2\frac{F_0}{\bar{s}}Y_\alpha^{(BA)}, \end{aligned}$$

where

$$S = \omega^{(A)} + \omega^{(B)},$$

$$J_{\alpha\xi\beta}^{(BA)} = \sum_{n\neq B}^{N^{(A)}}\hat{d}_\alpha^{(nA)}\hat{d}_\beta^{(nA)}\hat{d}_\xi^{(nA)},$$

and

$$Y_\alpha^{(BA)} = \sum_{n\neq B}^{N^{(A)}}\hat{d}_\alpha^{(nA)}.$$

Moment equilibrium for particle A is

$$0 = 6\pi\mu a K_{\alpha\beta}^{(BA)} v_{\beta}^{(BA)} \varepsilon_{\alpha\rho} \hat{d}_{\rho}^{(BA)} \; - 9.54\pi\mu a^2 \left(\hat{t}_{\beta} D_{\beta\xi} \hat{d}_{\xi}\right) + \pi\mu a^2 \left[\ln\left(\frac{a}{s^{(BA)}}\right) - 0.96\right] \omega^{(A)}$$
$$+\pi\mu a^2 \ln\left(\frac{a}{s^{(BA)}}\right) \omega^{(B)} + \varepsilon_{\alpha\rho} \sum_{n\neq B}^{N^{(A)}} \left\{ \frac{3}{\bar{s}} a^2 \pi\mu \left(D_{\beta\xi} \hat{d}_{\xi}^{(nA)} \hat{d}_{\beta}^{(nA)}\right) \hat{d}_{\alpha}^{(nA)} + \pi\mu a^2 \left[\ln\left(\frac{a}{\bar{s}}\right) - 0.96\right] \omega^{(A)} \hat{t}_{\alpha}^{(nA)} \right\} \hat{d}_{\rho}^{(nA)}$$
$$+\varepsilon_{\alpha\rho} \sum_{n\neq B}^{N^{(A)}} \left\{ 2a^2 \pi\mu \left[\ln\left(\frac{1}{\bar{s}}\right) - 0.96\right] \left(D_{\beta\xi} \hat{t}_{\xi}^{(nA)} \hat{d}_{\beta}^{(nA)}\right) \hat{t}_{\alpha}^{(nA)} - \frac{F_0}{\bar{s}} \hat{d}_{\alpha}^{(nA)} \right\} \hat{d}_{\rho}^{(nA)}. \tag{9.2}$$

A similar expression holds for particle B. The sum of moment equilibrium for particles A and B is

$$0 = 12\varepsilon_{\alpha\beta} K_{\alpha\mu}^{(BA)} v_{\mu}^{(BA)} \; \hat{d}_{\beta}^{(BA)} - 2 \times 9.54a \left(\hat{t}_{\mu}^{(BA)} D_{\mu\xi} \hat{d}_{\xi}^{(BA)}\right)$$
$$+a \left[2\ln\left(\frac{a}{s^{(BA)}}\right) - 0.96\right] S + a \left[\ln\left(\frac{a}{\bar{s}}\right) - 0.96\right] S\,(k-1)$$
$$+2a \left[2\ln\left(\frac{1}{\bar{s}}\right) - 1.92\right] \epsilon_{\xi\nu} A_{\nu\mu}^{(BA)} D_{\mu\xi}, \tag{9.3}$$

where

$$A_{\nu\mu}^{(BA)} = \sum_{n\neq B}^{N^{(A)}} \hat{d}_{\mu}^{(nA)} \hat{d}_{\nu}^{(nA)}.$$

In both the difference of force equilibrium and the sum of moment equilibrium, we have made the following approximations

$$A_{\nu\mu}^{(BA)} = A_{\nu\mu}^{(AB)},$$

$$J_{\alpha\xi\beta}^{(BA)} = -J_{\alpha\xi\beta}^{(AB)},$$

and

$$Y_{\alpha}^{(BA)} = -Y_{\alpha}^{(AB)}.$$

The projection of the difference in force equilibrium along the direction orthogonal to $t_{\alpha}^{(BA)}$ is

$$3\pi\mu a \frac{a}{s^{(BA)}} \dot{s}^{(BA)} - 2\frac{F_0}{s^{(BA)}} + 6\pi\mu a^2 \frac{a}{\bar{s}} \hat{d}_{\alpha} J_{\alpha\beta\gamma} D_{\beta\gamma} - 2\frac{F_0}{\bar{s}} Y_{\alpha} \hat{d}_{\alpha} = 0, \tag{9.4}$$

while the component along $t_{\alpha}^{(BA)}$is

$$0 = 12\pi\mu a K_{\alpha\beta}^{(BA)} v_{\beta}^{(BA)} t_{\alpha}^{(BA)} \; - 2 \times 9.54\pi\mu a^2 \left(\hat{t}_{\beta}^{(BA)} D_{\beta\xi} \hat{d}_{\xi}^{(BA)}\right)$$
$$+a^2\pi\mu \left[2\ln\left(\frac{a}{s^{(BA)}}\right) - 0.96\right] S + a^2\pi\mu \left[\ln\left(\frac{a}{\bar{s}}\right) - 0.96\right] S \varepsilon_{\alpha\beta} Y_{\beta}^{(BA)} t_{\alpha}^{(BA)}$$
$$+2\frac{3}{\bar{s}} a^2 \pi\mu D_{\beta\xi} J_{\alpha\xi\beta}^{(BA)} t_{\alpha}^{(BA)} + 2a^2\pi\mu \left[2\ln\left(\frac{1}{\bar{s}}\right) - 1.92\right] D_{\beta\xi} J_{\alpha\xi\beta}^{(BA)} t_{\alpha}^{(BA)}. \tag{9.5}$$

Using Eq. (9.5) and Eq.(9.3) , we solve for S:

$$S = -\frac{12b}{(4b-k+1)\,\bar{s}\,[\ln(1/\bar{s}) - 0.96]} \sin 2\theta,$$

or

$$S = -2c_2 \sin 2\theta, \tag{9.6}$$

where

$$c_2 = \frac{6b/\left[\bar{s}\left(4b - k + 1\right)\right]}{\ln\left(1/\bar{s}\right) - 0.96}.$$

10. Appendix B

The Matlab m-files for the numerical solution of the ordinary differential equations and boundary conditions follow.

```
function dydx = ODE(x,y,parameters,k,F,sbar,theta0)

% y(1)=s,  y(2)=A, y(3)=Int(A)
% k average number of contacts per particle; nu area fraction;
% F strength of repulsion, sbar average separation
% Interval: x from 0 to 1, theta1 is the parameter
% sol = bvp4c(@ODE,@BC,sol0,[],2.0,1e-4,0.02,1e-8)

alpha = -3*sqrt(3)*(k-1)/(16*pi);

theta1   = parameters(1,1);

deltheta = theta1-theta0;
theta    = theta0+deltheta*x;

s = y(1);

c1 = 4.77-3*alpha/sbar;
c2 = 6*alpha/(sbar*(4*alpha-k+1))*1/(log(1/sbar)-0.96);

sdot     = 2/3*F*(1+4*alpha*s/sbar)+2*alpha*s/sbar*2*cos(2*theta);
thetadot = (c1+c2*log(1/s))*sin(2*theta)/(log(1/s)+3.84);

ptdotdth = 2*thetadot*cot(2*theta);
ptdotds  = 1/(log(1/s)+3.84)*(1/s)*(thetadot-c2*sin(2*theta));
dtdotdth = ptdotdth+ptdotds*sdot/thetadot;

dsdth  = sdot/thetadot;
dAdth  = -y(2)*dtdotdth/thetadot;

dydx=[
      deltheta*dsdth  % s
      deltheta*dAdth  % A
      deltheta*y(2)   % Int(A)
     ];


function res = BC(ya,yb,parameters,k,F,sav,theta0)

% y(1)=s, y(2)=A, y(3)=Int(A)

theta1   = parameters(1,1);

res=[
     ya(1)-0.1. % sp(0)
     yb(1)-0.1  % sp(1)
     ya(3)      % Int Ap
     yb(3)-k/4  % Int Ap
    ];
```

This research was partially supported by the National Science Foundation under Grant No. NSF PHY-1748958 and by the Gruppo Nazionale della Fisica Matematica (Italy).

REFERENCES

Advani, S.G. & Tucker, C.L. 1987 The Use of Tensors to Describe and Predict Fiber Orientation in Short Fiber Composites. *J.Rheol.***31**, 751-784.

Advani, S.G. & Tucker, C.L. 1990 Closure approximations for three dimensional structure tensors. *J.Rheol.***34**, 367-386.

Ball, R. C. and Melrose, J. R. 1995 Lubrication breakdown in hydrodynamic simulations of concentrated colloids. *Adv. Colloid Interface Sci.***59**, 19-30.

Boyer, F., Guazzelli, E. and Pouliquen, O. 2011 Unifying Suspension and Granular Rheology. Phys. Rev. Lett. 107, 188301.

Brady, J. F. & Bossis, G. 1988 Stokesian dynamics. *Annu. Rev. Fluid Mech.* **20**(1), 111-157.

Goddard, J. D. 2006 A dissipative anisotropic fluid model for non-colloidal particle suspensions. *J. Fluid Mech.* **568**, 1-17.

Guazzelli, E. and Pouliquen, O. 2018 Rheology of dense granular suspensions. *J. Fluid Mech.* **852**, P1:1-73.

Jeffrey, D. J. 1992 The calculation of low reynolds number resistance functions for two unequal spheres.*Phys. Fluids A* **4**, 16-29.

Jeffrey, D. J. & Onishi, Y. 1984 Calculation of the resistance and mobility functions for two unequal rigid spheres in low-Reynolds-number flow. *J. Fluid Mech.* **139**, 261-290.

Jenkins, J. T., La Ragione, L., Johnson, D. & Makse, H.A. 2005 Fluctuations and effective moduli of an isotropic, random aggregate of identical, frictionless spheres *J. Mech. Phys. of Sol.* **53**, 197-225.

Jenkins, J.T. & La Ragione, L. 2015 An analytical determination of microstructure and stresses in a dense, sheared monolayer of non-Brownian spheres *J. Fluid Mech.* **763**, 218-236

Kraynik, A. M. and Reinelt, D. A. 1992 Extensional motions of spatially periodic lattices. *Int. J. Multiphase Flow* **18**, 1045-1059.

Love, A. E. H. 1944 A Treatise on the Mathematical Theory of Elasticity, Third Edition. Cambridge University Press, Cambridge.

Mari, R., Seto, R., Morris, J. F., Denn, M. M. 2014 Shear thickening, frictionless and frictional rheologies in non-Brownian suspensions *J. Rheol.* **58**, 1693-1724

Nazockdast, E. & Morris, J. F. 2012a Microstructural theory and rheology of concentrated suspensions. *J. Fluid Mech.* 713, 420-452.

Nazockdast, E. & Morris, J. F. 2012b Effect of repulsive interaction on structure and rheology of sheared colloidal suspensions.*Soft Matter* **8**, 4223-4234.

Nazockdast, E. & Morris, J. F. 2013 Pair-particle dynamics and microstructure in sheared colloidal suspensions: Simulation and Smoluchowski theory. *Phys. Fluids* **25**, 25070601.

Nott, P. R. and Brady, J. F. 1994 Pressure-driven flow of suspensions: simulation and theory *J. Fluid Mech.* 275, 157-199.

Onat, E.T. & Leckie, F.A. 1988 Representation of Mechanical Behavior in the Presence of Changing Internal Structure. *J. Appl. Mech.* **55**, 1-10

Phan-Thien, N.1995 Constitutive relation for concentrated suspensions in Newtonian liquids. *J. Rheol.* **39**, 679-695.

Prantil, V.C., Jenkins, J.T. and Dawson 1993 An analysis of texture and plastic spin for planar polycristal *J. Mech. Phys. of Sol.* **41**, 1357-1382.

Seto, R., Giusteri, and Martiniello, A. 2017 Microstructure and thickening of dense suspensions under extensional and shear flows. *J. Fluid Mech.* 825, xxx-yyy.

Seto, R., Mari, R., Morris, J. F., Denn, M. M. 2013 Discontinuous shear thickening of frictional hard-sphere suspensions *Phys. Rev. Lett.* 111, 218301

Sierou, A. & Brady, J. F. 2002 Rheology and microstructure in concentrated noncolloidal suspensions, *J.Rheol.* **46**, 1031-1056.

Singh, A. & Nott, P. R. 2000 Normal stresses and microstructure in bounded sheared suspensions via Stokesian Dynamics simulations. *J. Fluid Mech.* **412**, 279-301.

Stickel, J. J., R. J. Phillips & Powell, R. L. 2006 A constitutive model for microstructure and total stress in particulate suspensions. *J. Rheol.* **50**, 379-413.

Thomas, J.E., Ramola, K., Singh, A., Mari, R., Morris, J.F. and Chakraborty, B. 2018 Microscopic origin of frictional rheology in dense suspensions: correlations in force space. *Phys. Rev. Letts.* **121**, 128002.

Todd, B. D. and Daivis, P. J. 1998 Nonequilibrium Molecular Dynamics Simulations of Planar Elongational Flow with Spatially and Temporally Periodic Boundary Conditions *Phys. Rev. Lett.* **81**, 1118–1121

Torquato, S. 1995 Nearest-neighbor statistics for packings of hard spheres and disks. *Phys. Rev E*. **51**, 3170-3184.